

# Star formation history in the SMC: the case of NGC 602<sup>1</sup>

M. Cignoni<sup>2,3</sup>, E. Sabbi<sup>4,5</sup>, A. Nota<sup>4,5</sup>, M. Tosi<sup>3</sup>, S. Degl’Innocenti<sup>6,7</sup>, P.G. Prada Moroni<sup>6,7</sup>,  
L. Angeretti<sup>3</sup>, Lynn Redding Carlson<sup>8</sup>, J. Gallagher<sup>9</sup>, M. Meixner<sup>4</sup>, M. Sirianni<sup>4,5</sup>, L.J.  
Smith<sup>4,5,10</sup>

## ABSTRACT

Deep HST/ACS photometry of the young cluster NGC 602, located in the remote low density “wing” of the Small Magellanic Cloud, reveals numerous pre-main sequence stars as well as young stars on the main sequence. The resolved stellar content thus provides a basis for studying the star formation history into recent times and constraining several stellar population properties, such as the present day mass function, the initial mass function and the binary fraction. To better characterize the pre-main sequence population, we present a new set of model stellar evolutionary tracks for this evolutionary phase with metallicity appropriate for the Small Magellanic Cloud ( $Z = 0.004$ ). We use a stellar population synthesis code, which takes into account a full range of stellar evolution phases to derive our best estimate for the star formation history in the region by comparing observed and synthetic color-magnitude diagrams. The derived present day mass function for NGC 602 is consistent with that resulting from the synthetic diagrams. The star formation rate in the region has increased with time on a scale of tens of Myr, reaching  $0.3 - 0.7 \times 10^{-3} M_{\odot} yr^{-1}$  in the last 2.5 Myr, comparable to what is found in Galactic OB associations. Star formation is most complete in the main cluster but continues at moderate levels in the gas-rich periphery of the nebula.

*Subject headings:* galaxies: evolution-galaxies: star clusters-Magellanic Clouds-stars: formation-stars: pre-main sequence-open clusters and associations: individual (NGC 602)

---

<sup>1</sup> Based on observations with the NASA/ESA Hubble Space Telescope, obtained at the Space Telescope Science Institute, which is operated by the Association of Universities for Research in Astronomy (AURA), Inc., under NASA contract NAS5-26555. These observations are associated with program #10248.

<sup>2</sup>Dipartimento di Astronomia, Università degli Studi di Bologna, via Ranzani 1, I-40127 Bologna, Italy

<sup>3</sup>Istituto Nazionale di Astrofisica, Osservatorio Astronomico di Bologna, Via Ranzani 1, I-40127 Bologna, Italy

<sup>4</sup>Space Telescope Science Institute, 3700 San Martin Drive, Baltimore, USA

<sup>5</sup>European Space Agency, Research and Scientific Support Department, Baltimore, USA

<sup>6</sup>Dipartimento di Fisica “Enrico Fermi”, Università di Pisa, largo Pontecorvo 3, Pisa I-56127, Italy

<sup>7</sup>INFN - Sezione di Pisa, largo Pontecorvo 3, Pisa I-56127, Italy

<sup>8</sup>Department of Physics and Astronomy, Johns Hopkins University, Baltimore, USA

<sup>9</sup>University of Wisconsin, Madison, WI, USA

<sup>10</sup>Department of Physics and Astronomy, University Col-

## 1. Introduction

The Small Magellanic Cloud (SMC), the closest dwarf irregular galaxy, is the most appropriate target for detailed studies of resolved stellar populations in this extremely common class of objects. Its present-day metallicity ( $Z = 0.004$ ) makes the SMC the best local analog to the vast majority of late-type dwarfs. Deep optical photometry was performed on images from the Hubble Space Telescope (HST) Advanced Camera for Surveys (ACS) at different locations in the SMC as part of a program to study the global Star Formation History (SFH) of this galaxy and to understand how star formation is affected by local conditions such as metallicity and dust content. In the present paper, we derive the SFH for NGC 602, a very young cluster located in the “wing” of SMC. The NGC 602

---

lege London, Gower Street, London, UK

region offers a valuable laboratory to study infant stars (1-3 Myr) as well as billion year old objects. In particular, Carlson et al. (2007) identified a rich population of pre-main sequence (PMS) stars and candidate Young Stellar Objects (YSOs) using the Color-Magnitude Diagrams (CMDs) obtained from the HST optical data and Spitzer Space Telescope IR data. There is no question that the well defined stellar sequence, redder than the canonical main sequence is due to PMS stars. Conventional alternative explanations (reddening, binaries, photometric errors) have been taken into account but discarded because they fail to reproduce the CMD feature.

The discovery of low mass PMS stars in nearby galaxies (see also Romaniello et al. 2004; Nota et al. 2006; Gouliermis et al. 2007) is important for at least two reasons. First, it is an excellent benchmark for stellar evolution calculations, since it provides the opportunity to study rather large samples of PMS stars characterized by similar distance and chemical composition. Second, the detection of PMS stars with precise photometry gives an additional channel, with respect to the main sequence, to constrain the recent SFH: the short time spent in PMS by a  $1 M_{\odot}$  star ( $\sim 50$  Myr) roughly corresponds to the time spent by an  $8 M_{\odot}$  star on the main sequence, with the obvious advantage that stars of  $1 M_{\odot}$  are much more frequent than  $8 M_{\odot}$  stars.

The goal of this paper is to recover the SFH of NGC 602. For this task, we merged a well tested synthetic population code (Tosi et al. 1991) with an effective maximum likelihood technique (see e.g. Cignoni et al. 2006), to build accurate theoretical CMDs to be compared with the observations. The synthetic CMDs are generated by Monte Carlo sampling of canonical ingredients such as a star formation law, initial mass function (IMF), age-metallicity relation (AMR) and stellar evolution tracks. In order to properly account for the PMS phase, new PMS tracks at  $Z = 0.004$  have been calculated.

This paper is organized as follows. In section 2 the data are briefly described. In Section 3 we present the new set of PMS models. In Section 4 we disentangle the observed CMD in terms of age, metallicity, distance and reddening. In addition, the present day mass function (PDMF) is derived and some hypotheses on the interplay of the star

formation rate (SFR) with the environment are done. Section 5 is devoted to the method and the stellar ingredients we adopt for reconstructing the SFH. Finally, in section 6 we present our main quantitative results on the SFH.

## 2. Observations

For this project, we utilized observations of NGC 602 (R.A.=  $01^h29^m31^s$ , Dec=  $-73^{\circ}33'15''$ , J2000) taken with the Wide Field Channel (WFC) of the HST/ACS as part of proposal 10248 (P.I. A. Nota). Five long exposures were taken through filters F555W ( $\sim V$ ) and F814W ( $\sim I$ ). A dither pattern was especially designed to allow for hot pixel removal, and to fill the gap between the two halves of the  $4096 \times 4096$  pixel detector. This dithering technique also improved both point spread function (PSF) sampling and photometric accuracy by averaging flat-field errors and smoothing over the spatial variations in detector response. All the images were taken with a gain of  $2 e^{-}$  ADU $^{-1}$ . The entire data set was processed with the CALACS calibration pipeline, and for each filter the long exposures were co-added using the multi-drizzle package. The final exposure times of the deep combined F555W and F814W are 2150 s and 2265 s respectively. The image covers a region of  $200'' \times 200''$  corresponding to a linear size of  $58 \times 58 pc^2$  at the SMC distance (see Fig. 1 in Carlson et al. 2007).

Additional short B, V and I ground-based observations were taken with the camera ANDICAM on the 1.3 m Small and Moderate Aperture Research Telescope System (SMARTS), to recover the photometric information of the brightest stars, that are heavily saturated in the ACS data. Photometric observations included three 60 second B-band exposures, three 45 second V-exposures, and three 30 second I-exposures.

Figure 1 shows the ACS image of the region. In addition to the central cluster, two other sub-clusters are identified in the region, clearly separated from the central cluster. Following the nomenclature in Westerlund (1964), we call the central cluster NGC 602-A and the top-central sub-cluster NGC 602-B. The third sub-cluster is thereafter called NGC 602-B2 (corresponding to “cluster A” in Schmalzl et al. 2008).

As part of the same program we observed

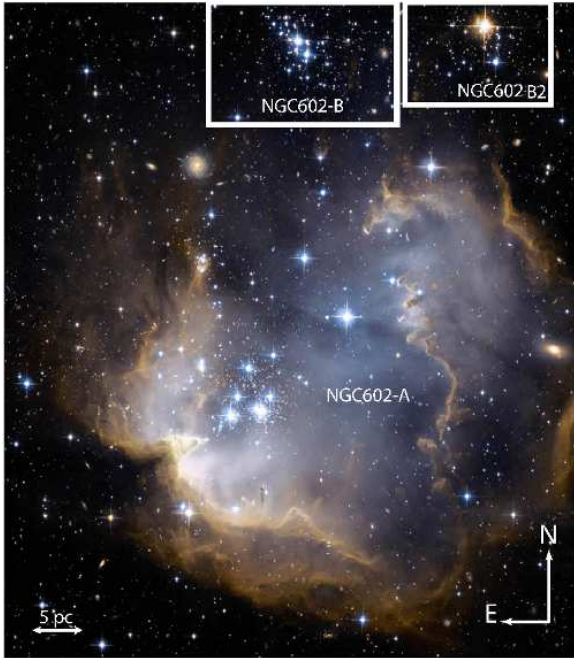


Fig. 1.— ACS image for the observed region around NGC 602. The sub-clusters NGC 602-B and NGC 602-B2 are also indicated.

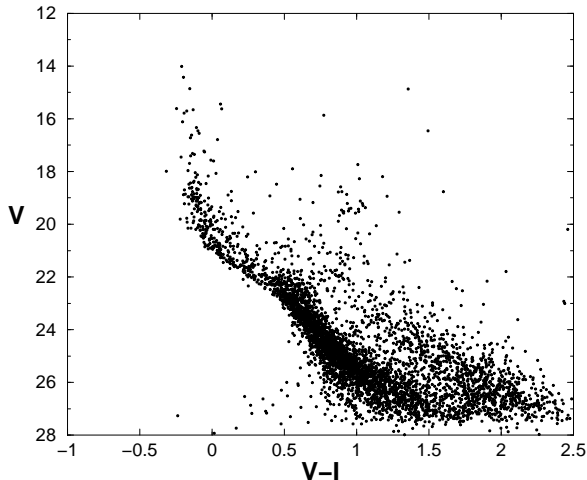


Fig. 2.— Optical Color Magnitude Diagram for the entire NGC 602 region.

NGC 602 core with the Near Infrared Camera and Multi Object Spectrometer (NICMOS). We used ACS in parallel to observe with the WFC a SMC reference field ( $\alpha = 01^h 29^m 19^s$ ;  $\delta = -73^\circ 42' 30.8''$ , J<sub>2000</sub>). The reference field is located  $\sim 9'46''$  ( $\sim 172$  pc) south from NGC 602. The data were analyzed following the same procedure described above, and used to subtract the contamination from the SMC field in the study of the present day mass function (PDMF, § 4.1).

## 2.1. Photometric Reduction

The photometric reduction has been performed with the DAOPHOT package within the IRAF<sup>1</sup> environment.

We have followed the same method used for NGC 330 (Sirianni et al. 2002) and NGC 346 (Sabbi et al. 2007a). To derive accurate photometry of all stars in the field, we adopted the PSF fitting and aperture photometry routines provided within DAOPHOT.

The stars in each image were independently detected using DAOFIND. We set the detection threshold to  $4\sigma$  above the background level in the F555W image and  $3.5\sigma$  in the F814W. We measured the stellar flux by aperture photometry with PHOT, and then refined the photometric measurements of the individual sources with PSF-fitting photometry. For both the F555W and F814W images we computed spatially variable PSFs by selecting more than 170 isolated and moderately bright stars, uniformly distributed over the images, in order to take into account the variations in shape and in core width of the PSF across the images (Krist 2003; Sirianni et al. 2005). Stars with  $m_{F555W} < 18$  and  $m_{F814W} < 17.5$  were discarded from the long exposure photometric catalog because they were saturated.

Many background galaxies are visible in the HST/ACS images (Nigra et al. 2008). For a safe interpretation of the characteristics of the observed stellar populations, we needed to distinguish true single stars from extended, blended and/or residual spurious objects such as background galaxies. Thus, we applied to our catalogs selection criteria based on the shape of the

<sup>1</sup>IRAF is distributed by the National Optical Observatories, which are operated by AURA Inc., under cooperative agreement with the National Science Foundation.

objects and on the quality of photometry. We considered the DAOPHOT parameters  $\chi^2$ , sharpness and photometric error  $\sigma_{\text{DAO}}$ .  $\chi^2$  gives the ratio of the observed pixel-to-pixel scatter in the fit residuals to the expected scatter calculated from a predicted model based on the measured detector features. The sharpness parameter sets the intrinsic angular size of the objects. We selected only the objects having  $-0.5 < \text{sharpness}_{m_{F555W}} < 0.5$  and  $-0.3 < \text{sharpness}_{m_{F814W}} < 0.3$ . These values turned out to be the best ones to allow us to reject background galaxies and fuzzy brightness variations in diffuse emission regions. Our HST catalog includes 4496 sources.

We used ground-based short V and I exposures to recover the photometric information of the saturated stars. We used the IRAF packages XREGISTER, IMSHIFT, and IMCOMBINE to properly align and combine the images in each band. We used DAOPHOT’s DAOFIND, with the detection threshold set at  $4\sigma$  from the background, to construct a photometry list. Stellar fluxes were measured by aperture photometry with an aperture size of 4 times the PSF FWHM, and then we refined the photometry by PSF-fitting. We used Landolt stars to calibrate the ground-based photometry into the Johnson-Cousins photometric system, and then we followed the prescription by Sirianni et al. (2005) to convert the photometric catalog into the Vegamag photometric system. The entire optical catalog includes 4537 stars calibrated in the HST Vegamag system. The resulting CMD is presented in Figure 2.

## 2.2. The Photometric Completeness

Reliable quantitative derivations of the evolutionary properties of the observed region require robust estimates of the photometric errors and incompleteness of our images. Spreads in the CMD sequences due to photometric errors could in fact mimic age, distance or reddening effects, and incompleteness competes with the SFH and the IMF in defining the observed luminosity functions.

In order to test the level of completeness of our photometric data and to have a more reliable estimate of the photometric errors and blending effects on our data, we run a series of extensive artificial star experiments, following the same procedure described in Sabbi et al. (2007b). The experiments consist of adding “artificial” stars, obtained

from the scaled PSF used in the photometric analysis of the frames, onto the actual image. Then the artificial stars are retrieved using exactly the same procedure adopted for the data reduction. The completeness is defined as the ratio between the stars retrieved and the stars added. In total, more than 1,000,000 artificial stars were simulated in the F555W and F814W deep exposures. The magnitudes of the artificial stars were chosen to mimic the observed distribution of stars in the CMD. Regions with no observed stars were assigned a minimum number of artificial stars to fully cover the CMD. We placed the artificial stars one at a time on a regular grid such that the spacing between them was 5.3 PSF-fitting radii (80 pixel), to ensure that the artificial stars experiments did not change the crowding conditions of the data. To fully sample the completeness level of the data, the absolute position of the grid with respect to the frame was randomly changed at each run.

The frame to which the artificial stars were added was reduced exactly as the original frame. We determined the level of photometric completeness by comparing the list of artificial stars “added” with the list of the stars “recovered”. In our experiments each star found contemporarily in both frames with an input-output magnitude difference  $\Delta m \leq 0.75$  and satisfying the selection criteria listed in §2.1 is considered a “recovered” star. The completeness factor as a function of magnitude for both filters F555W and F814W is presented in Figure 3. This completeness factor and the photometric errors derived here have been adopted to create the synthetic CMDs described in Sect.5.

## 3. Stellar tracks

The synthetic CMDs used to reconstruct the SFH of NGC 602 are calculated adopting suitable theoretical stellar tracks, from the PMS birthline to the AGB phase. For all the stellar phases except the PMS, we use the Padua evolutionary tracks (Fagotto et al. 1994). The PMS tracks are new and specifically computed with an updated version of the FRANEC evolutionary code (see e.g. Chieffi & Straniero 1989; Degl’Innocenti et al. 2007). For these models the OPAL 2006 equa-

tion of state (EOS)<sup>2</sup> has been adopted (see also Iglesias & Rogers 1996), together with radiative opacity tables by the Livermore group<sup>3</sup> (see also Iglesias & Rogers 1996) for temperatures higher than 12000°K; in this way the EOS and opacity calculations are fully consistent. The conductive opacities are from Shternin & Yakovlev (2006) (see also Potekhin 1999) while the atmospheric opacities are from Ferguson et al. (2005). All the opacity tables have been calculated adopting the Asplund & Grevesse (2005) solar mixture. Nuclear reaction rates are from the NACRE compilation (Angulo et al. 1999).

As is well known, the treatment of the early PMS phases is very problematic and the definition of the birth-line (that is the phase in which the proto-star reaches thermal and hydrostatic equilibrium and can be thus represented in a CMD) requires the adoption of hydrodynamical codes (see e.g. Wuchterl & Tscharnuter 2003; Stahler & Palla 2004, for an extensive analysis). In addition, the results are influenced by several physical parameters still not well known (the accretion rate, the deuterium mass fraction in the interstellar medium, and the stellar opacity, see e.g. Bernasconi 1996) and thus the analysis can be only semi-quantitative. As a general procedure in stellar evolutionary codes, our calculations artificially start from a total convective model at the hydrostatic and thermal equilibrium. However this should not constitute a problem: numerical simulations have already shown that the stellar characteristics after the birth-line are not significantly influenced by the previous evolutionary history. The birth-line is supposed to be reached very early (our synthetic CMDs are built with a birth-line at 0.5 Myr, which is fairly compatible with the data CMD) and thus, at least for masses that are not too high ( $< 5 - 6 M_{\odot}$ ), the greater part of the PMS evolution can be represented in the CMD.

Models have been calculated with  $Z=0.004$   $Y=0.24$  and the mixing-length parameter  $\alpha = 1.9$  for masses in the range  $0.45 - 5.5 M_{\odot}$  (all PMS models are presented in Table 1a). Fig. 4 shows our computed PMS tracks in the theoretical Luminosity-Temperature plane.

<sup>2</sup>[http://www-phys.llnl.gov/Research/OPAL/EOS\\_2005/](http://www-phys.llnl.gov/Research/OPAL/EOS_2005/)

<sup>3</sup>[http://www-phys.llnl.gov/Research/OPAL/EOS\\_2005/](http://www-phys.llnl.gov/Research/OPAL/EOS_2005/)

To convert all stellar tracks (Padua and Pisa) from the Luminosity-Temperature plane to the CMD we used the transformations by Origlia & Leitherer (2000) for the HST Vegamag photometric system. The transformed PMS tracks are shown in Fig. 5.

#### 4. General considerations from the CMD analysis

Although the most striking feature is the presence of a wealth of PMS stars, the CMD also shows a clear signature of an old population. In particular, we see a main sequence (MS) turn-off (TO) near  $M_{F555W} \sim 22$ , a sub-giant branch (SGB) also at  $M_{F555W} \sim 22$ , and a red clump (RC) around  $M_{F555W} \sim 19.5$ . Excluding a large contamination by PMS stars more massive than  $1.5 M_{\odot}$ , this is likely due to the SMC field population, still present also in these low-density “wing” areas. A contamination of the SGB by high mass PMS stars cannot be ruled out. From the evolutionary point of view, the presence of PMS stars indicates a SF activity in the last few million years, while the width of the upper main sequence suggests an overall activity in the last 100 Myr. The RC represents a population older than 500 Myr burning helium in the stellar core and the SGB at that luminosity level indicates that stars of several Gyr are present in our sample - likely the SMC field population.

Fig. 6 shows isochrone fitting of the young stellar population using Padua stellar models for  $Z=0.004$ , corrected for distance ( $m - M)_0 = 18.9$  and reddening  $E(B - V) \sim 0.08$ . In the magnitude range  $V = 15 - 19$  a stellar excess is observed on the red side of the isochrones. We exclude the possibility that this is a pure age effect. In fact, although aging the youngest stars by some Myr would move the bright end of the main sequence to the red, it would have also the collateral effect of producing an unobserved blue-shift of the PMS population. We consider it more likely that our sample be affected by significant differential reddening, with some of the brighter stars more reddened than the faint ones. If these stars are actually the massive counterpart of the observed faint PMS, these stars can be still surrounded by relics of their birthing cocoon material and suffer an additional amount of absorption. Another possibility is that some of the most massive stars are rotating. In this case, these stars would be shifted

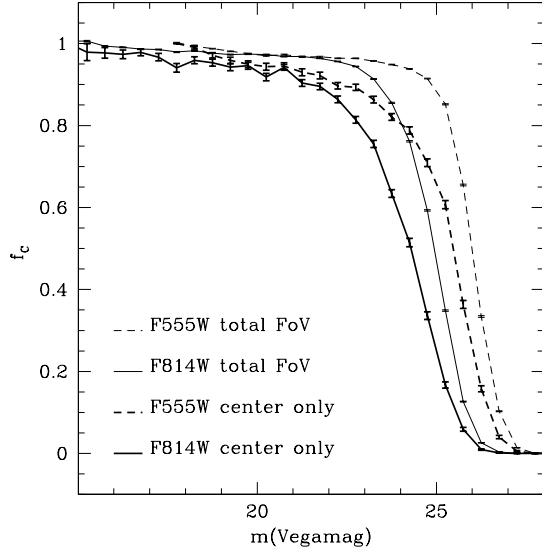


Fig. 3.— Completeness curves as derived from the artificial star experiment for the F555W (*dashed line*) and F814W (*solid line*) photometry as a function of magnitude. Completeness curves have been derived both for the entire field of view (narrow lines) and for the central region only (thick lines).

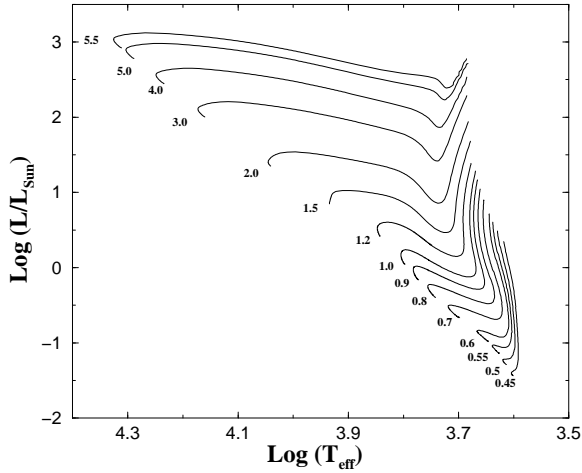


Fig. 4.— PMS evolutionary tracks for  $Z = 0.004$ , where the characteristic mass for each track is given, in solar masses.

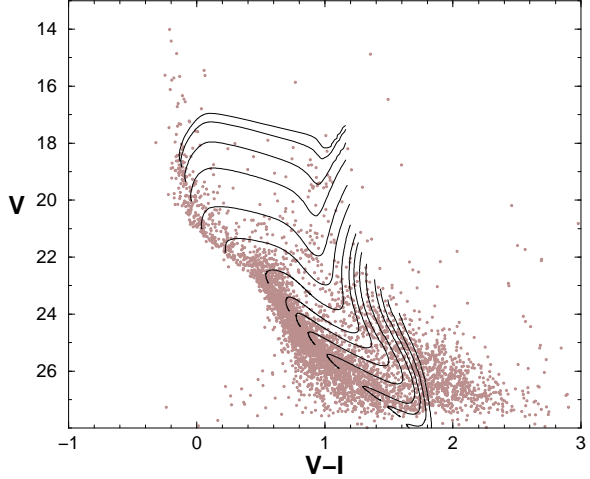


Fig. 5.— FRANEC PMS stellar tracks ( $Z = 0.004$ ) overlaid on the observed CMD.

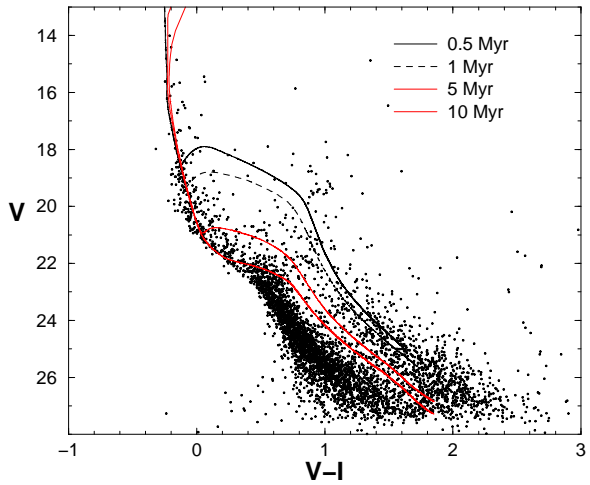


Fig. 6.— 0.5, 1.0, 5.0 and 10.0 Myr isochrones for metallicity  $Z = 0.004$  interpolated from the Padua tracks and FRANEC tracks for PMS overlaid on the observed CMD. Distance modulus and reddening are assumed equal to  $(m - M)_0 = 18.9$  and  $E(B - V) \sim 0.08$ , respectively.

to lower effective temperatures as a consequence of the lower internal pressure with respect to non-rotating ones (see e.g. Meynet & Maeder 2000).

Besides the upper main sequence, the PMS population gives constraints on our age estimates. Fig. 5 shows the observed CMD with the PMS tracks (masses from 0.45 to 5.5  $M_{\odot}$ ) for metallicity  $Z = 0.004$  over-plotted. It is clear that the theoretical tracks comfortably encompass the red sequence, confirming the pre-main sequence nature of these sources. Even more interesting, the bulk of these stars seem to lie in the Hayashi region. Figure 6 shows the corresponding PMS isochrones for 0.5 Myr, 5 Myr and 10 Myr, and suggests that most of the PMS stars are younger than 5 Myr. The same Figure underlines the effectiveness of the PMS stars as astrophysical clocks: the upper main sequence alone is degenerate with respect to progressive epochs of recent star formation, and it is impossible to resolve isochrones of different ages. In contrast, the same epochs of star formation are clearly separated in the PMS region that, therefore, offers a more accurate snapshot of the star formation activity in the last 50 Myr.

A further inspection of the PMS region reveals that, at least for  $V > 23$ , many objects are up to 1 magnitude redder than our PMS tracks. The number of these red stars is too large to ascribe them to photometric errors. More likely some very young objects continue to have significant amounts of dust, thus suffering additional self-absorption (see also Section 6.1.4 for a discussion).

One additional question is whether the sub-clusters NGC 602-B and NGC 602-B2 have a different history to the central active region (NGC 602-A). Figure 7 shows the CMD for the stars found in the boxes<sup>4</sup> of Figure 1, chosen to represent NGC 602-B and NGC 602-B2. Both clusters are reproduced using isochrones with ages between 15 and 150 Myr, slightly older than NGC 602 ( $\sim 10$  Myr). It must be emphasized however that this difference in age is due to only one and two stars evolved off the MS in NGC 602-B and NGC 602-B2 respectively. Due to the low number of stars the sub-clusters NGC 602-B and

NGC 602-B2 are indistinguishable from NGC 602-A. In other words, the same star formation process that took place on various scales in the whole region spawned also these two small associations.

Looking for ancient populations, Figure 7 shows also that a well-defined SGB along with a RC is a common feature of the CMD for NGC 602-A, B and B2. This finding is a robust indicator of an old population, being the SGB and the RC phases populated by low mass stars. Moreover, the compact morphology of the RC suggests that the metallicity does not vary in the sample in a relevant way.

By means of isochrone fitting, we find that luminosities and colors of RC and SGB can be simultaneously reproduced by assuming a metallicity of  $Z = 0.001$ , a distance modulus  $(m - M)_0 = 18.9$ , reddening  $E(B - V) \sim 0.08$ , and an age between 4 and 8 Gyr (see Fig. 8).

#### 4.1. The Present Day Mass Function

From an observational point of view, the mass function (MF) is the fractional number of stars per mass interval per unit area. Here we adopt the parameterization by Scalo (1986), in which the mass function is characterized by a slope  $\Gamma = d\xi(\log m)/d\log m$ , where  $m$  is the mass, and  $\xi(\log m)$  is the number of stars born per unit logarithmic mass interval. In this parameterization, the MF for the solar neighborhood, as derived by Salpeter (1955) has a slope  $\Gamma = -1.35$ .

The MF of a system is empirically inferred by counting the number of stars in mass intervals. As shown in previous sections, in NGC 602 the star formation occurred over a long interval of time, and it is likely still ongoing. In these conditions, we cannot infer the initial mass function (IMF) from the observational data without making assumptions on how the SFR varies with time. Therefore in this section we discuss only the present day mass function (PDMF) for those stars that are already visible in the optical bands, but have not evolved yet off the main sequence.

To derive the PDMF of NGC 602 we applied the same technique discussed in Sabbi et al. (2007b). This technique has the advantage of avoiding assumptions on the age of the stellar population and therefore overcomes the age/luminosity degeneracy which affects young star forming regions. It

<sup>4</sup>Although the shape of these selection areas may lead to overestimate the field stars, the aim here is only to investigate the stars around the two overdensities (whose boundaries may be quite irregular).

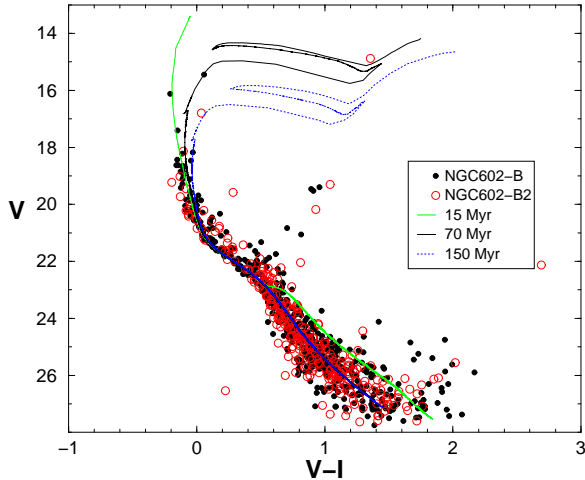


Fig. 7.— Isochrones overlaid on the CMD for the regions of NGC 602-B and NGC 602-B2.

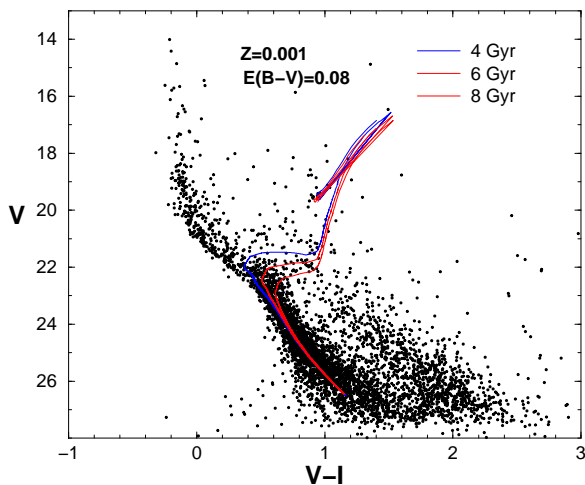


Fig. 8.— 4.0, 6.0 and 8.0 Gyr Padua isochrones for  $Z = 0.001$  (Angeretti et al. see 2007) at the distance modulus  $(m - M)_0 = 18.9$  and reddening  $E(B - V) = 0.08$  superimposed on the observed CMD.

simply consists of directly counting the stars between two theoretical evolutionary tracks (Fig. 5). In particular, to measure the PDMF for stars more massive than  $6 M_{\odot}$  we used Padua evolutionary tracks, while we used the FRANEC PMS tracks at lower masses.

NGC 602 is a relatively small star cluster, and its upper main sequence appears poorly populated. As pointed out by Maíz Apellániz & Úbeda (2005), in such conditions, the size of the mass bin might affect the slope of the measured MF, artificially increasing its steepness. To be conservative, we divided the brightest part of the CMD into only two bins, each containing the same number of stars.

As already done for NGC 346 (Sabbi et al. 2007b), we took into account the completeness variations as a function of magnitude and color by dividing into bins of 0.5 in magnitude and 0.25 in color, the stars identified between two evolutionary tracks. We then normalized the number of stars lying within two evolutionary tracks to the logarithmic width of the mass range spanned by the tracks and to the area of the observed region, and then we applied the appropriate completeness factor.

To remove the contamination of the SMC stellar population in our data, we considered a SMC field ( $\alpha = 01^h 29^m 15.9^s$ ,  $\delta = -73^{\circ} 42' 30''$ ), located at a projected distance of  $\sim 47$  pc from NGC 602 and observed with the F555W and F814W filters of the ACS/WFC. For each mass bin, the estimated number of stars belonging to the field of the SMC was subtracted from the PDMF. We therefore derived the NGC 602 PDMF between  $0.7$  and  $30 M_{\odot}$  (Fig. 9). Using a weighted least mean squares fit of the data, we derive a slope  $\Gamma = -1.25 \pm 0.22$  ( $\alpha = 2.25$ ) for the PDMF of NGC 602, in agreement with Schmalzl et al. (2008). Uncertainties may still affect the derived slope of the PDMF. These include the percentage of unresolved binary systems, possible variable extinction, underestimating the mass for the most massive stars, etc. For example, if we consider the extreme case of a 30% fraction of equal mass ratio unresolved binaries, the slope of the PDMF becomes  $\Gamma = -1.48 \pm 0.17$ .



## 4.2. The Environment

The compelling questions we are addressing in this paper are how star formation started and progressed in this region. Do we observe evidence of sequential star formation or of mass segregation? How do star formation and environment mutually affect each other?

It would be tempting to explain the origin of the gas shells clearly visible in the true image (see Fig.1) as due to massive stellar winds and/or supernovae explosions, but this turns out not to be the case. Nigra et al. (2008) used HST images and high-resolution echelle spectra from the Anglo-Australian Telescope (AAT), together with HI survey data, to study the immediate vicinity of NGC 602 in some detail. They find that NGC 602 was probably formed  $\sim 7$  Myr ago as a result of the compression and turbulence associated with the interaction of two expanding H I shells. The AAT optical spectroscopy shows that the ionized gas close to the central cluster and within the H II region N90 is quiescent. This suggests that a supernova explosion has yet to occur within NGC 602, and that the winds from the massive stars are not sufficient to drive rapid expansion of the HII region, although they have produced a hot, X-ray emitting medium within NGC 602 (Oskinova, private communication). Nigra et al. (2008) therefore conclude that the H II region seen in Fig. 1 has been shaped by the ionizing radiation from the massive stars in the central cluster. In particular, the wealth of fine structure appears to be the result of the ionization front eroding dense, neutral, clumpy material. This picture is consistent with the idea that the ionizing radiation from the central cluster photo-evaporated the residual gas, causing star formation to cease in the central regions, while it is still ongoing in the dense, outer neutral material.

We have studied the spatial distribution of the youngest and of the most massive stars in the region. First, we examined the young stars identified by comparing the observed CMD with theoretical isochrones. In Fig. 10, red dots indicate PMS stars, younger than 5 Myr, with masses between 0.5 and 1.5  $M_{\odot}$ . Most of these stars are concentrated in the core of the central cluster and along several filamentary structures. Interestingly, this population is almost absent in the two sub-clusters

NGC 602-B and NGC 602-B2. A first obvious conclusion is that NGC 602-B and NGC 602-B2 are slightly older than NGC 602-A. As already mentioned above, we do not have enough stars to infer if NGC 602-A, B and B2 are or not coeval, however it is clear that the three regions had significantly different SFRs.

Figure 10 shows also the position (yellow large circles) of stars more massive than 8  $M_{\odot}$  in any evolutionary phase. These stars have formed in the last 50 Myr or so. They are mostly concentrated in the center, but several are scattered outside the central cluster, we can therefore conclude that we are not seeing evidence of mass segregation in this cluster. Given the relatively young age of the central cluster, it is also appropriate to infer that the massive stars are formed in situ, since the cluster has not had enough time to undergo any dynamical evolution.

To understand the progression of star formation in the region, it is also fundamental to note the result of Carlson et al. (2007), who found, from Spitzer data, a generation of class 0.5 - I YSO (age  $10^4 - 10^5$  yr) located at the outskirts of the central cluster, along the dusty ridges. Carlson et al. (2007) concluded that star formation started at the center of the cluster and likely propagated outwards, with star formation still ongoing in the outer dusty regions.

In order to investigate the relation, if any, of the recent star formation activity with the current stellar density we have divided the region around NGC 602-A in bins of  $200 \times 200$  pixels ( $10'' \times 10''$ ) and counted the number of stars in each bin. The bins have then been grouped according to their number of stars: bins with more than 30 stars are defined as R1, those with 20-30 stars as R2, those with 10-20 stars as R3, and those with less than 10 stars as R4. The spatial distribution of the four density intervals is shown in the top panel of Figure 11, where individual stars are plotted with different symbols. Stars in the highest density bins R1 are represented by red dots, stars in R2 by orange asterisks, stars in R3 by green dots, and stars in R4 by black open circles. This map suggests the presence of a high density region concentrated on NGC 602-A, surrounded by filamentary structures of decreasing stellar density and super-imposed on a rather homogeneous field, with minimum density, possibly corresponding to the SMC

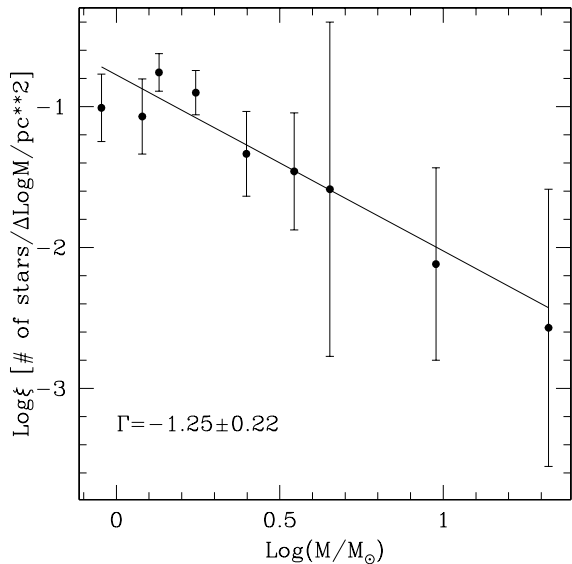


Fig. 9.— Derived NGC 602 PDMF.

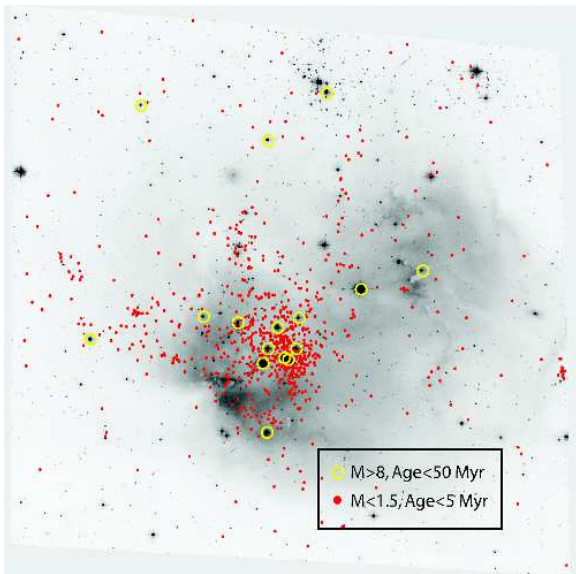


Fig. 10.— Young stars of masses above  $8 M_{\odot}$  (yellow circles) and PMS of masses below  $1.5 M_{\odot}$  (red dots) are superimposed on the finding chart derived from Figure 1. Masses are deduced by isochrones fitting from Fig. 6. The plotted massive stars are younger than 50 Myr and the PMS younger than 5 Myr.

background.

The CMDs corresponding to each of the four density intervals are presented in the other panels of Fig. 11. The 5 Myr isochrone is also plotted for reference in each panel. These CMDs clearly show that the high density regions R1 and R2 are dominated by PMS stars, whose distribution is tight and close to the 5 Myr isochrone, whilst very few PMS stars are detected in the lowest density region R4 (black dots). If we consider the number of PMS per unit area, we find that the PMS density drops by a factor of 70-80 from R1 to R4 (the corresponding density ratios from R1 to R2 and R3 being respectively 3 and 14). At first glance, the lower main sequence appears instead more populated moving from high to low-density regions. However, once the star counts are normalized to the area, we find that the main sequence density drops too, although only by a factor 1.5-2. While the PMS stars show a clear trend of decreasing density with increasing distance from the center of NGC 602-A, the MS only shows a discontinuity between the external, low density region R4 and all the others, which have MS densities similar to each other. We interpret the moderate discontinuity in MS density from R4 to the denser regions as due to the simultaneous contribution of field plus cluster MSs in R2-3-4.

The clear star density gradient indicates that the recent SF rate has been higher in the central regions. However, when we take into account that the 25 *bona fide* YSOs identified by Carlson et al. (2007) are found on the gas rims and are absent in the more central regions, we need to conclude that the most recent SF activity has occurred at the outskirts of the cluster. This suggests that the SF activity has stopped earlier in the center than in the periphery of the cluster, probably because of the higher gas consumption rate.

## 5. Synthetic CMDs: the approach

Synthetic stellar populations are generated to reproduce the observed CMD. The synthetic CMD is created following the procedure originally described by Tosi et al. (1991) and subsequently updated (Greggio et al. 1998; Angeretti et al. 2005): 1) stellar masses and ages are randomly chosen from a time independent Initial Mass Function and a star formation law, respectively; 2) an as-

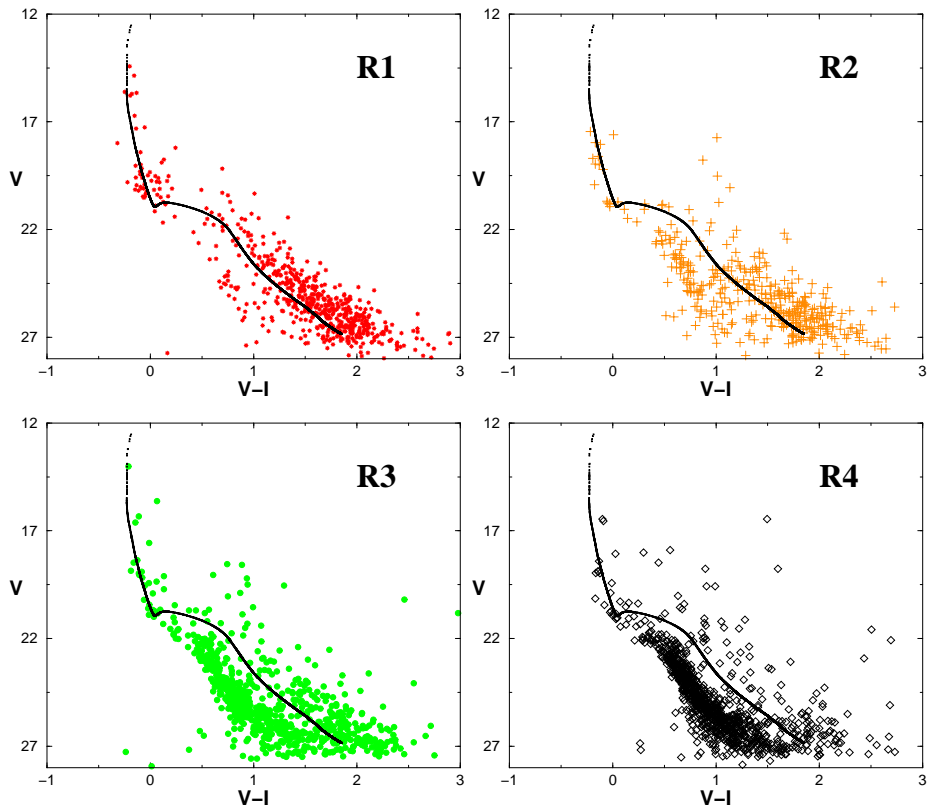
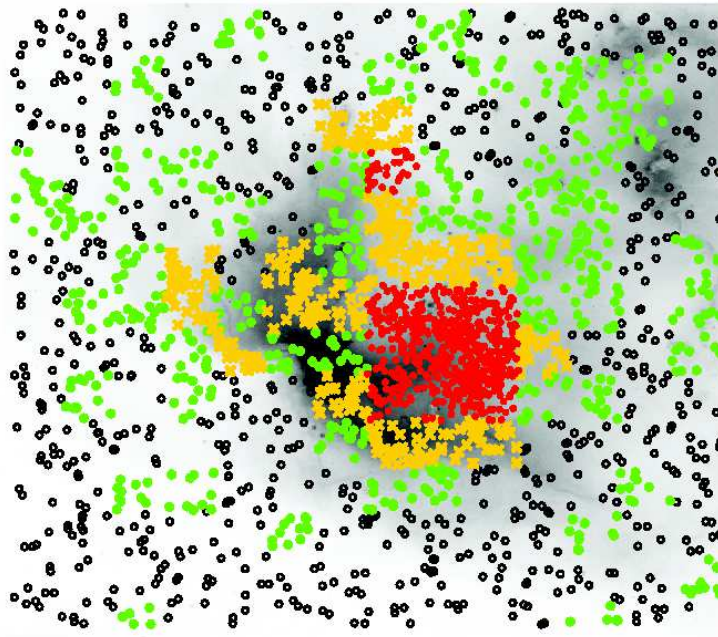


Fig. 11.— Top panel: XY map of NGC 602-A and its neighborhood. The different colors represent different constant density surfaces (see text). Lower panels show the separate CMDs of the four density regions. From R1 to R4 the stellar crowding decreases.

sumed age-metallicity relation provides the metallicity; 3) stellar tracks ranging from pre-main sequence to asymptotic giant branch phase are interpolated, deriving the absolute photometry for the synthetic population; 4) distance, reddening, incompleteness and photometric errors are applied. Once a synthetic CMD is created, we apply a maximum likelihood classification algorithm as presented in Cignoni et al. (2006) in order to make a rigorous comparison with the observations. To evaluate the goodness of the assumed model, observational and theoretical CMDs are converted into two dimensional histograms by dividing the CMDs in cells ( $0.1 \times 0.1$  mags) and counting the stars in each cell. Once the number of theoretical and observational objects is known in each cell, we implement a function of the residuals (Poissonian  $\chi^2$ ) to quantify the differences between the two histograms. This function is minimized by means of a downhill simplex algorithm. In order to avoid local minima, the simplex is re-started from thousands of initial random positions. A bootstrap method is used to assess a confidence around the best parameters. The entire process is repeated for each bootstrapped data set. The error bars represent the mean deviation using 100 bootstrap. For a detailed description of this procedure see Cignoni et al. (2006).

In order to reduce the computational time, the star formation rate is parameterized as a set of constant values over adjacent temporal intervals. Each constant star formation produces a partial CMD (a quas-single stellar population) and a generic star formation history can be written as a linear combination of the partial CMDs. The advantage of a similar procedure is that a library of partial CMDs is built (see Figure 12) just once, in advance, and the genesis of any additional SFH is reduced to elementary algebraic combinations. Finding the best SFH means searching for the combination of partial CMDs which minimizes the  $\chi^2$ .

Disentangling a stellar population showing both very recent (Myr) and very old (Gyr) episodes of star formation is not straightforward. Only low mass stars will survive from ancient episodes because their evolutionary timescales are very long: small CMD displacements, for example due to photometric errors, can bias the age estimates up to some Gyr. In this case, increasing the time res-

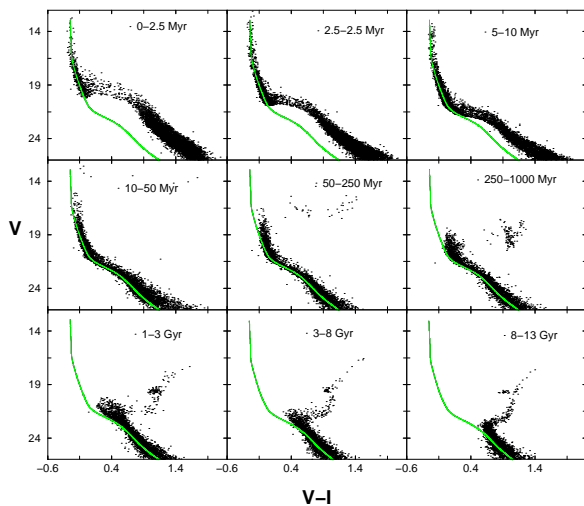


Fig. 12.— Synthetic partial CMDs for the labeled time interval, with 30% of unresolved binaries being assumed. The continuous line is the zero age main sequence (ZAMS). Upper three panels: the star formation activity is younger than 10 Myr and consequently most of the stars are still in PMS (only massive stars are in main sequence). As expected, aging the system (moving from the left panel to the right panel) shifts the *turn-on* point (where the PMS stars reach the main sequence) to progressively fainter magnitudes. Middle three panels: most of the stars have reached the main sequence and some massive stars have evolved off (core helium burning stars). Lower panels: the oldest star formation steps. Here also intermediate mass stars (roughly  $M > 1M_{\odot}$ ) have evolved off the main sequence.

olution, besides being time-consuming, may produce unrealistic star formation rates due to misinterpretation. Hence, the choice of temporal resolution must follow both the time scale of the underlying stellar populations and the data scatter (photometric errors, incompleteness, etc.). Given the overall recent activity of our field, a practical way out is to use a coarser temporal resolution for the older epochs, which: 1) allows us to avoid SFH artifacts at early epochs; 2) reduces the Poisson noise; 3) reduces the parameter space. In our simulations the duration of each step is progressively increased with age as labeled in Figure 12.

## 6. Recovering the star formation history

Following the prescriptions of Section 5 and the population properties described in Section 4 we assume that objects younger than 3 Gyr are formed with metallicity  $Z = 0.004$ , and that the older ones are formed with  $Z = 0.001$ . For all synthetic stars, a distance modulus  $(m - M)_0 = 18.9$  and reddening  $E(B - V) \sim 0.08$  are assumed. Before exploring different IMF exponents and binary recipes, the SFH is searched starting from an arbitrary power-law IMF ( $\phi(m) \propto m^{-\alpha}$ ) and binary fraction and then letting them vary. At the end of the iterations, the best SFH turned out to have  $\alpha=2.5$  and a binary fraction of 30% (companion masses are picked randomly from the same IMF). Our result is shown in Figure 13. The maximum activity is reached in the last 2.5 Myr (about  $0.3 \times 10^{-3} M_{\odot} yr^{-1}$ ). This phenomenon is also confirmed through a visual inspection of the CMD morphology. The PMS phase is well separated from the main sequence, suggesting that most of the PMS stars are moving down their own Hayashi tracks. Looking back in time, the star forming activity drops by a factor approximately 2 between 2.5 and 5 Myr ago and a factor of 10 between 10 Myr and 50 Myr ago. Beyond this epoch, it drops again by another factor of 10, but slightly increasing around 6-8 Gyr ago. Finally, the period between 8 and 13 Gyr ago is characterized by a very low activity, confirming that the bulk of the oldest stars in our field have ages of about 8 Gyr.

In spite of the fact that the stronger star formation activity is extremely recent, most of the stellar mass budget (the total mass of all stars

ever born in our field, i.e., the integral of the star formation history) was forged into stars at earlier epochs. Considering only stars more massive than  $0.45 M_{\odot}$ , the NGC 602 field has produced about  $4400 M_{\odot}$  in the last 3 Gyr, while as much as  $8000 M_{\odot}$  were converted into stars between 3 and 13 Gyr ( $7000 M_{\odot}$  between 3 and 8 Gyr ago). Looking at Figure 10 we see that stars younger than 5 Myr are confined in a surface of roughly  $10 \times 10 pc^2$ : considering that the mean SFR in the last 5 Myr is about  $0.22 \times 10^{-3} M_{\odot} yr^{-1}$ , it implies a recent star formation rate density of  $2.2 \times 10^{-6} M_{\odot} yr^{-1} pc^{-2}$  (i.e.  $2.2 \times M_{\odot} yr^{-1} kpc^{-2}$ ). Extrapolating the IMF down to the hydrogen burning limit ( $\sim 0.1 M_{\odot}$ ) with the same slope, this number increases to  $4.8 \times 10^{-6} M_{\odot} yr^{-1} pc^{-2}$ , while no significant variations exist if the IMF flattens below  $0.45 M_{\odot}$  (Kroupa 2001 finds  $\alpha = 1.3 \pm 0.5$ ).

The CMD corresponding to our best SFH is shown in the bottom panel of Fig.14. The top panel of the same Figure shows the observed CMD for a direct comparison.

### 6.1. The robustness of the SFH

In order to check the robustness of the resulting SFH, it is important to carry out a stability analysis. Indeed, our result has been obtained under specific assumptions on secondary parameters (IMF, binary fraction, distance and reddening), which are intrinsically poorly known. We dedicate the next sections to quantifying the influence on the recovered SFH by these uncertainties. The distance modulus of the young population is varied in the range 18.7-18.9. For the IMF we have tested  $\alpha$  values between 2 and 3 (Salpeter's being 2.35); for the binary stars we have assumed fractions from 20 % to 70 %.

#### 6.1.1. Distance

While the luminosity of the red clump allows us to tightly constrain the distance modulus of the old population at 18.9, the distance of the NGC 602 young cluster remains more uncertain because of the MS spread. A distance modulus of 18.7 would better match the location of the young population in the CMD. This value would place the cluster slightly in front of the SMC, confirming that this object is a member of the "wing". In

Fig.15 we show together the two SFHs derived for the two adopted values of the distance modulus, namely 18.7 and 18.9. It is evident that the SFH is only weakly affected by the slight change in this parameter.

### 6.1.2. IMF

To assess how the recovered SFH is influenced by the IMF, the star formation is re-determined adopting different IMF exponents, assuming in this case a fixed binary population of 30%. Figure 16 shows that the mean SFH systematically increases with steepening IMF. In fact, for a fixed total mass, a shallower IMF implies fewer stars surviving in the final sample (because the IMF flattening causes a deficit of low-mass long-lived stars), hence a higher SFH is required to produce the observed star counts.

The overall trend of the SF activity with time does not change significantly, though, varying at most by a factor smaller than 2. We can thus conclude that the recovered SFH is quite robust against IMF variations.

We also tried to further constrain the IMF exponent. However, instead of adding an extra free parameter (the IMF exponent) in the whole procedure to infer the SFH, only the best SFHs of Figure 16 has been explored further. In particular, we tested which IMF exponent produces, within the Poisson noise, acceptable star counts in relatively large color-magnitude boxes (see Figure 17). We map those stellar phases which are especially sensitive to the IMF (for example, the ratio between the star counts from the upper main sequence stars and the PMS is extremely sensitive to the IMF slope).

With respect to the likelihood method, this strategy allows a strong improvement in statistics. As a further check, the luminosity function for synthetic stars brighter than  $V = 24$  has been compared with the observational luminosity function.

Our results show that the luminosity functions built with an IMF exponent  $\alpha = 2.5$  are nicely within the Poisson error bars (see Fig. 18). The small size of our sample makes it difficult to firmly establish which value is best for the exponent. Testing different  $\alpha$ 's, however, we have found that only values between 2.1 and 2.7 are acceptable (see

Figs. 19 and 20). For values higher than 2.7, the bright main sequence population falls short of what is observed, while IMFs flatter than  $\alpha = 2.1$  result in an over-populated upper main sequence.

### 6.1.3. Binaries

In this section we analyze the influence on the resulting SFH of the assumed fraction of unresolved binaries. Partial CMDs have been generated with 20%, 30%, 50% or 70% of unresolved binary systems (for each binary, primary and secondary masses are both randomly extracted from the same IMF).

Concerning PMS stars, some observations seem to suggest a higher binary fraction with respect to field stars. The Taurus star forming region in the Milky Way has a factor of two excess of binaries, although other regions show no excess. There is no consensus yet on the origin of this phenomenon. Analyses of binary fractions in young open clusters suggest that no evolutionary effect (leading to binary disruption) is at work (at least after 50-70 Myr). Environmental effects provide a more convincing explanation: the apparent overabundance of young companions in Taurus with respect to the solar neighborhood might imply that the SF in low-stellar-density regions such as Taurus is particularly efficient to produce multiple systems, and that such regions are not primary progenitors of our solar neighborhood. However, the current sensitivity cannot exclude that the discrepancy arise from an observational bias: the low mass companions are brighter in PMS than in main sequence, making the detection easier. Given these uncertainties, we prefer to adopt the same binary fraction for all evolutionary phases.

Figure 21 shows the recovered SFHs: the overall effect of increasing the binary fraction is a degradation of the information on the SFH, washing out some features, both in recent and in past epochs. This is because both the main sequence and the PMS region are broadened by the presence of binaries, blending contiguous temporal intervals.

Unlike the IMF, changing the fraction of binaries does not introduce a systematic deviation; the effect is localized to specific epochs. Binaries produce a secondary sequence redder and brighter than the single star main sequence. When the

stars evolve, they turn to the red and in this sense a binary system may be confused with an evolved single star. But, a binary system is also brighter, thus, it may be also confused with a higher mass star (corresponding in main sequence to a younger age). Even if the effect of binaries is quite complex, our numerical results are comforting: the recovered SFH is not significantly affected by this assumption.

In order to put some limits on the number of binaries in our field, the synthetic CMDs are generated using the SFHs of Figure 21 and the luminosity functions are further explored. Our analysis suggests that any fraction lower than 70% is equally acceptable because the photometric error smears out the single and binary star sequences and makes them indistinguishable from each other.

A visual inspection of the CMD allows additional considerations. Fig. 22 (top panel) shows the CMD for a binary fraction of 50%. Compared to the CMD generated with a 30% (Fig. 14), the turn-off region around  $V \sim 22$  appears broader, better matching the observations. However, since the same color spread can be obtained through many other ingredients (rotation, stronger overshooting, reddening, metallicity, etc.), we do not see compelling evidence to prefer this specific value.

To be conservative, only binary fractions larger than 70% (bottom panel) can be easily discarded. As visible in the bottom panel of Fig. 22 the synthetic CMD assuming such large fractions lacks the observed color separation between lower main sequence and PMS.

#### 6.1.4. Additional uncertainties regarding the PMS phase

In addition to the “classical” uncertainties, some specific issues are expected to affect only the PMS phase (see e.g. Sherry 2003). First of all, low-mass PMS stars are often identified as highly variable stars, so called T Tauri-stars. Their large amplitude irregular variations in the brightness are believed to arise from accretion shocks on the stellar surface and/or chromospheric flaring. This effect, still not well understood, can contribute to smearing the CMD in the PMS region, mimicking an age spread. Differential reddening, which pref-

erentially affects stars still embedded in gas and dust like the PMS stars, should also be considered as another plausible source of confusion. Several studies have tried to evaluate the impact of these uncertainties on the CMD. Studying OB associations like  $\sigma$  Orionis, Burningham et al. (2005) argue that the combination of variability (on a typical period of a few years) and differential reddening can produce, at most, an age spread of 4 Myr. This spread is of the same order of magnitude as the result of Hennekemper et al. (2008) for the NGC346 region (another SMC star forming region), who find that a combination of binarity/variability/reddening might smear out any SFH feature (as deduced from PMS alone) in the last 10 Myr. However, these estimates may be an upper limit. In fact, there is a growing evidence for large differences in the accretion disk (that is the first candidate for variability and absorption in T-Tauri stars) dissipation timescales for stars of a given mass in OB associations: a fraction around 30% appears to lack the disk at 1 Myr, while the remainder hold accretion disks up to ages of  $\sim 10 - 20$  Myr. Additional uncertainties are also the position of the birth-line, which is strongly correlated with the number of T-Tauri, and the treatment of convection, which is parameterized assuming a mixing length parameter as derived from the Sun.

The lack of information about these uncertainties is so high that we do not attempt to include them in the models. Moreover, these uncertainties affect only the PMS, while we use all stellar phases to derive the SFH.

## 7. Discussion and Conclusions

In this paper, we presented a detailed look at the stellar content of an SMC region (NGC 602), characterized by extremely low gas and dust density, but displaying the properties of a very active and complex star forming environment.

NGC 602 is located in the SMC “wing”, and its stellar population is a mixture of extremely young stars, born in the last few million years, and very old stars, likely belonging to the SMC field population, of age 6-8 Gyr. The young population is preferentially found in the densest central region. A rich population of PMS stars is observed, which appear still to be descending their Hayashi tracks.

This sets the maximum age for these stars at 5 Myr. In addition, the central region of the cluster shows an excess of PMS and low mass main sequence stars. If we add the compelling evidence (Carlson et al. 2007) that the star formation is currently ongoing along the outskirts of the central cluster, where a significant number of YSOs have been observed in Spitzer/IRAC images, the following scenario looks most attractive:

- an intense star formation activity began deep in the main cluster, NGC 602-A;
- a less intense star formation process propagated or continued outside;
- the activity has already stopped inside, while outside it is still smoldering.

Using a metallicity  $Z = 0.004$  (consistent with the most recent determinations for the SMC), we derive a distance modulus  $(m - M)_0 = 18.9$  and a reddening  $E(B - V) = 0.08$  for NGC 602. However, a visible red shift of the upper main sequence with respect to the models could imply that the youngest stars are affected by stronger reddening, and therefore the distance modulus could decrease to  $(m - M)_0 = 18.7$ , consistent with the fact that NGC 602 is located in the SMC “wing”.

The old population is more uniformly distributed. Using a metallicity  $Z = 0.001$  and the same distance/reddening combination as the young population, we can simultaneously well reproduce the observed data for the lower sub-giant branch and the helium clump color/luminosity. A higher metallicity would require a much lower reddening, inconsistent with the Schlegel maps that indicate  $E(B - V) = 0.06$ .

With the objective of understanding how star formation started and progressed in this region, we have used the detailed census of the stellar content to derive the star formation history for NGC 602.

First of all, on the basis of the observational data, we estimated the PDMF. Our results indicate that in the mass range between 0.7 and 30  $M_\odot$  the PDMF slope is  $\Gamma = -1.25 \pm 0.22$  (see also Schmalzl et al. 2008), and becomes  $\Gamma = -1.48 \pm 0.17$  if we consider a 30% fraction of unresolved binaries. We inferred a very similar value for the IMF of NGC 602 ( $\Gamma_{IMF} = -1.5$ ) using the synthetic CMD method including binaries. Both our estimates are in excellent agreement with the value

derived by Salpeter in the solar neighborhood. Therefore, despite the extremely low gas and dust density, star cluster formation and evolution do not seem to be significantly affected by the local conditions. We have used the measured PDMF to derive the total mass in the NGC 602 region. By integrating the observed PDMF between 0.7 and 120  $M_\odot$ , we calculate a total mass for NGC 602 of 1600  $M_\odot$ , indicating that the star formation event was quite modest in size.

Nigra et al. (2008) have addressed the issue of what triggered the initial episode of star formation in this region. They identified a distinct HI cloud component that is likely the progenitor cloud of the cluster and present HII region. From HI survey data, they measured a HI density in the natal cloud of  $1.3 \text{ cm}^{-3}$  and a total mass of  $3 \times 10^5 M_\odot$  based on a scale size of 220 pc. This would imply an observed star formation efficiency lower than 1%, as typically expected.

We have used our population synthesis model to analyze the SFH of the region. We have adopted the new PMS tracks for  $Z = 0.004$  computed with the FRANEC evolutionary code, and presented in this paper. We have assumed different choices for IMF and binary fraction, to test the robustness of our results. The best SFH is derived using a maximum likelihood technique. We note that the derived SFHs turn out to be qualitatively rather similar, independent of the assumptions on the IMF or binary fraction, confirming the robustness of the result. The star formation activity has been increasing with time on a time scale of tens of Myr. The star formation in the recent 10 Myr has been quite high, reaching a peak of  $(0.3 - 0.7) \times 10^{-3} M_\odot/\text{yr}$  (the exact value depends on the IMF extrapolation) in the last 2.5 Myr. The current star formation is approximately 100 times higher than the average from 4-8 Gyr ago. Any activity older than 8 Gyr ago seems to be negligible.

These results highlight the two different generations in the region: the recent one, increasing in the near past and still ongoing, very spatially concentrated, and the several Gyr old one, spatially diffused and related to the SMC field.

We can assemble the results of Nigra et al. (2008) and this paper to compose a plausible scenario for the formation and evolution of this region. The SMC experienced a first intense episode of SF in this region several Gyr ago ( $\sim 6 - 8$ ),



followed by a long period of moderate activity. Only approximately 10 Myr ago, the compression and turbulence associated with the interaction of two HI shells caused a progressive increase in the local star formation rate, that reached  $0.3 \times 10^{-3} M_{\odot} yr^{-1}$  in the recent 2.5 Myr, and led to the formation of the central cluster NGC 602-A. Star formation is still ongoing in the remaining reservoirs of gas/dust at the outskirts of the cluster and it is likely to continue at the same pace until the fuel is totally exhausted.

It is not straightforward to compare our rate with those of similar OB associations. However,  $(0.3 - 0.7) \times 10^{-3} M_{\odot} yr^{-1}$  seems in good agreement with the results for several, relatively small scale, star forming regions. For example, Preibisch & Zinnecker (2000) find for the Upper Scorpius association in the Milky Way a star formation rate of  $10^{-3} M_{\odot} yr^{-1}$  on a projected radius of 10-15 pc. These stars formed almost coevally about 5-6 Myr ago (Preibisch & Zinnecker 2000).

A similar intensity in star formation is also found in the Orion Nebula: Hillenbrand & Hartmann (1998) report  $10^{-4} - 10^{-3} M_{\odot} yr^{-1}$  within a projected radius of 2.5 pc. The mean age is younger than 6 Myr. However, while the star forming activity in the Orion Nebula has stopped, the NGC 602 region shows clear evidence of YSOs, a signature that the process has not completely exhausted the fuel yet. Lada, Alves & Lada (1996) find for NGC1333, an active region (probably younger than 2 Myr) in the Perseus cloud, a star formation rate of  $4 \times 10^{-5} M_{\odot} yr^{-1}$ .

Although the NGC 602 star formation rate appears quite similar to other young star clusters, it is much smaller than the stellar production in 30 Doradus, a “starburst-like” complex in LMC: for this region, Kennicutt (1998) suggests rates of  $10^{-2} M_{\odot} yr^{-1}$  in a region of 10 pc, with a similar age of 3 Myr.

The remote location, the low density of gas and dust, and the quiescence of the SMC wing are not favorable to star formation. Still NGC 602 is displaying activity that is very comparable to known galactic young star clusters, further confirming our understanding that local conditions have little effect on the stellar content, for example, in terms of the distribution of masses (MF). Remarkably our multi-wavelength approach allowed us to look

back in history at the very origin of this region, and follow the various phases of its evolution.

The expectation is that for NGC 602 the exciting times are still to come when the bulk of the massive stars will explode as SNeII and will significantly perturb the local medium.

## Acknowledgments

We are grateful to P. Montegriffo for his software support, and to Howard Bond for acquiring the SMART data. L.A., M.C. and M.T. acknowledge financial support from PRIN-INAF-2005. Support for program #10248 was provided by NASA to the US team members through a grant from the Space Telescope Science Institute, which is operated by AURA, Inc., under NASA contract NAS 5-26555. JSG also thanks the University of Wisconsin Graduate School for partial support of this research.

## REFERENCES

- Angeretti, L., Tosi, M., Greggio, L., Sabbi, E., Aloisi, A., Leitherer, C., 2005, *AJ*, 129, 2203
- Angeretti, L., Fiorentino, G., & Greggio, L. 2007, *IAU Symposium*, 241, 41
- Angulo C. et al., 1999, *Nucl. Phys.*, 3, 187
- Asplund, M., Grevesse, N., & Sauval, A.J. 2005, in “Cosmic Abundances as Records of Stellar Evolution and Nucleosynthesis”, eds. F.N. Bash, & T.J. Barnes, *ASP Conf. Series*, 336, 25
- Bernasconi, P. A. 1996, *A&AS*, 120, 57
- Burningham, B., Naylor, T., Littlefair, S. P., Jeffries, R. D., 2005, *MNRAS*, 363, 1389
- Carlson, L.R., Sabbi, E., Sirianni, M., Hora, J., Nota, A., Meixner, M., Gallagher, J.S., Oey, M.S., Pasquali, A., Smith, L.J., Tosi, M., Walterbos, R. 2007, *ApJ*, 665, L109
- Chieffi A., & Straniero O., 1989, *ApJS*, 71, 47
- Cignoni, M., Degl’Innocenti, S., Prada Moroni, P. G. & Shore, S. N., 2006, *A&A*, 459, 783
- Degl’Innocenti S., Prada Moroni P. G., Marconi M. & Ruoppo A., 2007, *Astrophysics and Space Science*, Online First

- Fagotto, F., Bressan, A. Bertelli, G., & Chiosi, C. 1994, *A&AS*, 105, 29
- Ferguson, J. W., Alexander, D. R., Allard, F., et al. 2005, *ApJ*, 623, 585
- Gouliermis, D. A., Henning, T., Brandner, W., Dolphin, A. E., Rosa, M. & Brandl, B., 2007, 665, 27
- Greggio, L., Tosi, M., Clampin, M., de Marchi, G., Leitherer, C., Nota, A. & Sirianni, M., 1998, *ApJ*, 504, 725 Gouliermis, D.A., Quanz, S.P., & Henning, T. 2007, *ApJ*, 665, 306
- Hennekemper, E., Gouliermis, D. A., Henning, T., Brandner, W., Dolphin, A. E., 2008, *ApJ*, 672, 914
- Hillenbrand, L.A., & Hartmann, L.W. 1998, *ApJ*, 492, 540
- Iglesias, C., & Rogers, F.J., 1996, *ApJ*, 464, 943
- Kennicutt, R. C., 1998, *ARA&A*, 36, 189
- Krist, J.E. 2003, ACS Ist. Sci. Rep 2003-06 (Baltimore: STScI)
- Kroupa, P. 2001, *MNRAS*, 322, 231
- Lada, C. J., Alves, J., & Lada, E. A. 1996, *AJ*, 111, 1964
- Maíz Apellániz, J., & Úbeda, L. 2005, *ApJ*, 629, 873
- Meynet, G., & Maeder, A. 2000, *A&A*, 361, 101
- Nigra, L., Gallagher, J. S., Smith, L.J., Stanimirovic, S., Nota, A., Sabbi, E., 2008, *AJ*, (accepter for publication) astro-ph/0808.1033
- Nota, A., et al. 2006, *ApJ*, 640, L29
- Origlia, L., & Leitherer, C. 2000, *AJ*, 119, 2018
- Potekhin A.Y., 1999, *A&A*, 351, 787
- Preibisch & Zinnecker 2000
- Romaniello, M., Scuderi, S., Panagia, N., Salerno, R. M. & Blanco, C., 2006, *A&A*, 446, 955
- Romaniello, M., Robberto, M., & Panagia, N. 2004, *ApJ*, 608, 220
- Sabbi, E., Sirianni, M., Nota, A., Tosi, M., Gallagher, J., Meixner, M., Oey, M.S., Waltherbos, R., Pasquali, A., Smith L.J., & Angeretti, L. 2007a, *AJ*, 133, 44
- Sabbi, E., Sirianni, M., Nota, A., Tosi, M., Gallagher, J., Smith, L.J., Angeretti, L., Meixner, M., Oey, M.S., Waltherbos, R., & Pasquali, A. 2007b, *AJ*(in–press), astro-ph0710.0558
- Salpeter, E.E. 1955, *ApJ*, 121, 161
- Scalo, J.M. 1986, *Fund. Cosmic. Phys.*, 11, 1
- Schlegel, D. J., Finkbeiner, D. P., & Davis, M. 1998, *ApJ*, 500, 525
- Schmalzl, M., Gouliermis, D. A., Dolphin, A. E., Henning, T., 2008, *ApJ*, 681,290
- Sherry, W. H., 2003, PhD thesis, SUNY , Stony Brook**
- Shternin, P.S. & Yakovlev, D.G., 2006, *PhRvD*, 74, (4) 3004
- Sirianni, M., Nota, A., De marchi, G., Leitherer, C., & Clampin, M. 2002, *ApJ*, 579, 275
- Sirianni, M., et al. 2005, *PASP*, 117, 1049
- Stahler, S.W., & Palla, F. 2004, “The Formation of Stars”, New York, Wiley
- Tosi, M., Greggio, L., Marconi, G., Focardi, P., 1991, *AJ*, 102, 951
- Westerlund, B.E. 1964, *MNRAS*, 127, 429
- Wuchterl, G., & Tscharnuter, W. M. 2003, *A&A*, 398, 1081
- de Zeeuw, P. T., Hoogerwerf, R., de Bruijne, J. H. J., Brown, A. G. A., & Blaauw, A. 1999, *AJ*, 117, 354

TABLE 1A  
PMS TRACKS ( $Z=0.004$ ,  $Y=0.24$ ).

Age (yr)	$\text{Log}(L/L_{\odot})$	$\text{Log}(T_{\text{eff}})$	Age(yr)	$\text{Log}(L/L_{\odot})$	$\text{Log}(T_{\text{eff}})$	Age(yr)	$\text{Log}(L/L_{\odot})$	$\text{Log}(T_{\text{eff}})$
0.45 $M_{\odot}$			0.50 $M_{\odot}$			0.60 $M_{\odot}$		
0.10E+05	0.337	3.618	0.10E+05	0.475	3.629	0.10E+05	0.694	3.645
0.20E+05	0.316	3.617	0.20E+05	0.449	3.629	0.20E+05	0.661	3.645
0.30E+05	0.295	3.617	0.30E+05	0.425	3.629	0.30E+05	0.630	3.644
0.50E+05	0.258	3.616	0.50E+05	0.381	3.628	0.50E+05	0.577	3.644
0.70E+05	0.224	3.615	0.70E+05	0.343	3.627	0.70E+05	0.531	3.644
0.10E+06	0.179	3.614	0.10E+06	0.292	3.625	0.10E+06	0.473	3.643
0.20E+06	0.065	3.610	0.20E+06	0.164	3.621	0.20E+06	0.332	3.640
0.30E+06	-0.018	3.607	0.30E+06	0.074	3.618	0.30E+06	0.234	3.637
0.40E+06	-0.082	3.605	0.40E+06	0.005	3.615	0.40E+06	0.158	3.634
0.50E+06	-0.135	3.604	0.50E+06	-0.051	3.613	0.50E+06	0.094	3.631
0.60E+06	-0.179	3.603	0.60E+06	-0.098	3.612	0.60E+06	0.043	3.629
0.70E+06	-0.218	3.602	0.70E+06	-0.139	3.610	0.70E+06	-0.001	3.628
0.80E+06	-0.252	3.601	0.80E+06	-0.175	3.609	0.80E+06	-0.039	3.626
0.10E+07	-0.310	3.600	0.10E+07	-0.235	3.608	0.10E+07	-0.104	3.623
0.20E+07	-0.495	3.597	0.20E+07	-0.425	3.603	0.20E+07	-0.304	3.617
0.30E+07	-0.605	3.596	0.30E+07	-0.538	3.601	0.30E+07	-0.420	3.614
0.50E+07	-0.748	3.594	0.50E+07	-0.682	3.600	0.50E+07	-0.565	3.611
0.70E+07	-0.844	3.593	0.70E+07	-0.777	3.599	0.70E+07	-0.658	3.610
0.10E+08	-0.945	3.592	0.10E+08	-0.876	3.598	0.10E+08	-0.750	3.609
0.20E+08	-1.136	3.592	0.20E+08	-1.057	3.598	0.20E+08	-0.891	3.614
0.30E+08	-1.237	3.592	0.30E+08	-1.142	3.601	0.30E+08	-0.924	3.623
0.50E+08	-1.336	3.595	0.50E+08	-1.209	3.608	0.50E+08	-0.845	3.656
0.10E+09	-1.394	3.604	0.10E+09	-1.238	3.620	0.10E+09	-0.970	3.647
0.18E+09	-1.437	3.601	0.15E+09	-1.288	3.613	0.11E+09	-0.968	3.647
0.70 $M_{\odot}$			0.80 $M_{\odot}$			0.90 $M_{\odot}$		
0.10E+05	0.868	3.655	0.10E+05	1.007	3.662	0.10E+05	1.116	3.667
0.20E+05	0.827	3.655	0.20E+05	0.960	3.662	0.20E+05	1.065	3.668
0.30E+05	0.791	3.655	0.30E+05	0.919	3.663	0.30E+05	1.021	3.669
0.50E+05	0.730	3.655	0.50E+05	0.852	3.664	0.50E+05	0.949	3.671
0.70E+05	0.678	3.655	0.70E+05	0.796	3.664	0.70E+05	0.891	3.671
0.10E+06	0.615	3.655	0.10E+06	0.728	3.665	0.10E+06	0.821	3.672
0.20E+06	0.464	3.654	0.20E+06	0.572	3.664	0.20E+06	0.661	3.673
0.30E+06	0.362	3.652	0.30E+06	0.468	3.663	0.30E+06	0.557	3.672
0.40E+06	0.285	3.650	0.40E+06	0.389	3.662	0.40E+06	0.478	3.671
0.50E+06	0.222	3.648	0.50E+06	0.326	3.660	0.50E+06	0.415	3.670
0.60E+06	0.169	3.646	0.60E+06	0.274	3.659	0.60E+06	0.363	3.670
0.70E+06	0.124	3.645	0.70E+06	0.228	3.658	0.70E+06	0.317	3.669
0.80E+06	0.084	3.643	0.80E+06	0.188	3.656	0.80E+06	0.277	3.668
0.10E+07	0.017	3.640	0.10E+07	0.120	3.654	0.10E+07	0.210	3.666
0.20E+07	-0.199	3.630	0.20E+07	-0.096	3.645	0.20E+07	-0.002	3.658
0.30E+07	-0.320	3.625	0.30E+07	-0.222	3.639	0.30E+07	-0.119	3.654
0.50E+07	-0.462	3.622	0.50E+07	-0.358	3.635	0.50E+07	-0.239	3.654
0.70E+07	-0.547	3.621	0.70E+07	-0.428	3.636	0.70E+07	-0.283	3.660
0.10E+08	-0.624	3.622	0.10E+08	-0.475	3.642	0.10E+08	-0.274	3.677
0.20E+08	-0.624	3.639	0.20E+08	-0.359	3.698	0.20E+08	-0.021	3.759
0.30E+08	-0.565	3.682	0.30E+08	-0.224	3.752	0.30E+08	-0.142	3.776
0.50E+08	-0.607	3.709	0.44E+08	-0.395	3.742	0.35E+08	-0.163	3.773
0.74E+08	-0.654	3.700						
1.00 $M_{\odot}$			1.20 $M_{\odot}$			1.50 $M_{\odot}$		
0.10E+05	1.224	3.671	0.10E+05	1.330	3.679	0.10E+05	1.585	3.683
0.20E+05	1.167	3.673	0.20E+05	1.275	3.681	0.20E+05	1.507	3.686
0.30E+05	1.119	3.674	0.30E+05	1.229	3.682	0.30E+05	1.447	3.688
0.50E+05	1.041	3.676	0.50E+05	1.154	3.685	0.50E+05	1.354	3.692
0.70E+05	0.980	3.677	0.70E+05	1.095	3.686	0.70E+05	1.285	3.694
0.10E+06	0.906	3.678	0.10E+06	1.024	3.688	0.10E+06	1.204	3.697
0.20E+06	0.742	3.680	0.20E+06	0.864	3.690	0.20E+06	1.032	3.701
0.30E+06	0.636	3.680	0.30E+06	0.760	3.691	0.30E+06	0.924	3.703
0.40E+06	0.557	3.679	0.40E+06	0.683	3.692	0.40E+06	0.846	3.705
0.50E+06	0.494	3.679	0.50E+06	0.621	3.692	0.50E+06	0.784	3.705
0.60E+06	0.442	3.678	0.60E+06	0.569	3.692	0.60E+06	0.735	3.706
0.70E+06	0.396	3.678	0.70E+06	0.526	3.692	0.70E+06	0.693	3.707
0.80E+06	0.357	3.677	0.80E+06	0.488	3.691	0.80E+06	0.658	3.707
0.10E+07	0.290	3.675	0.10E+07	0.424	3.691	0.10E+07	0.602	3.708
0.20E+07	0.085	3.670	0.20E+07	0.244	3.691	0.20E+07	0.476	3.718
0.30E+07	-0.022	3.668	0.30E+07	0.170	3.695	0.30E+07	0.485	3.734
0.50E+07	-0.112	3.674	0.50E+07	0.166	3.716	0.50E+07	0.782	3.782
0.70E+07	-0.119	3.687	0.70E+07	0.275	3.745	0.70E+07	1.022	3.888
0.10E+08	-0.045	3.717	0.10E+08	0.530	3.794	0.10E+08	0.861	3.934
0.20E+08	0.191	3.804	0.16E+08	0.417	3.843	0.12E+08	0.850	3.934
0.27E+08	0.046	3.797						
2.00 $M_{\odot}$			3.00 $M_{\odot}$			4.00 $M_{\odot}$		
0.10E+05	1.815	3.689	0.10E+05	2.122	3.695	0.10E+05	2.329	3.697
0.20E+05	1.726	3.693	0.20E+05	2.016	3.701	0.20E+05	2.219	3.705
0.30E+05	1.658	3.696	0.30E+05	1.941	3.705	0.30E+05	2.141	3.710
0.50E+05	1.558	3.701	0.50E+05	1.832	3.710	0.50E+05	2.037	3.716
0.70E+05	1.485	3.704	0.70E+05	1.756	3.714	0.70E+05	1.970	3.721
0.10E+06	1.401	3.707	0.10E+06	1.672	3.718	0.10E+06	1.908	3.726

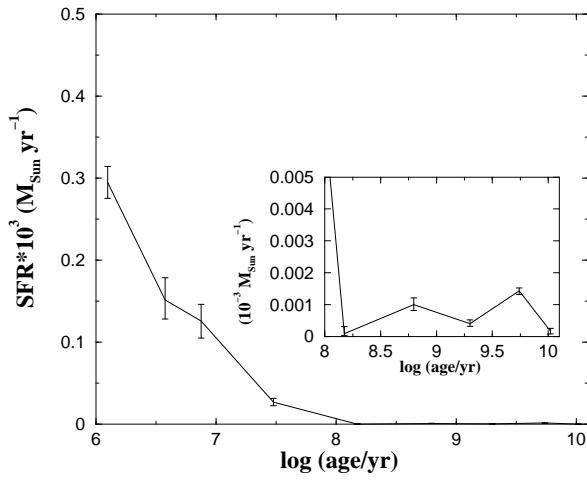


Fig. 13.— Recovered star formation rate using an IMF exponent  $\alpha = 2.5$  and a binary fraction of 30%. The old star formation activity is enlarged in the small panel.

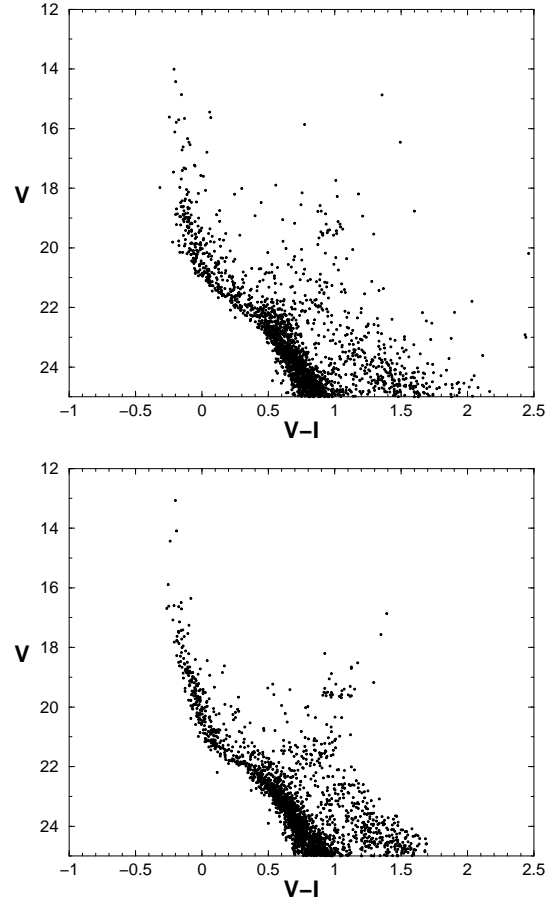


Fig. 14.— Up: Observational CMD. Bottom: Best synthetic CMD. It is obtained assuming an IMF exponent  $\alpha = 2.5$ , a binary fraction of 30% and the SFH of Fig. 13.

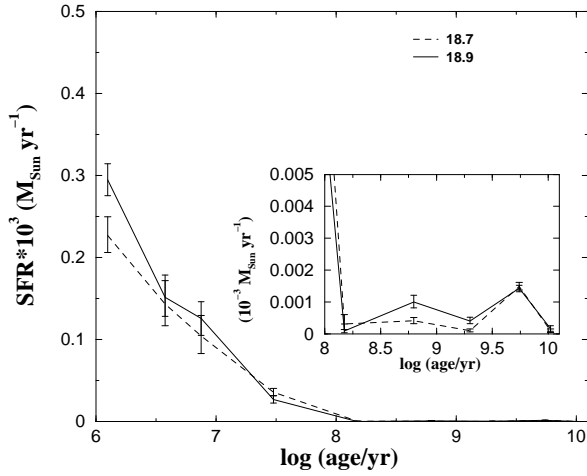


Fig. 15.— Recovered SFH for two choices of the young population distance modulus.

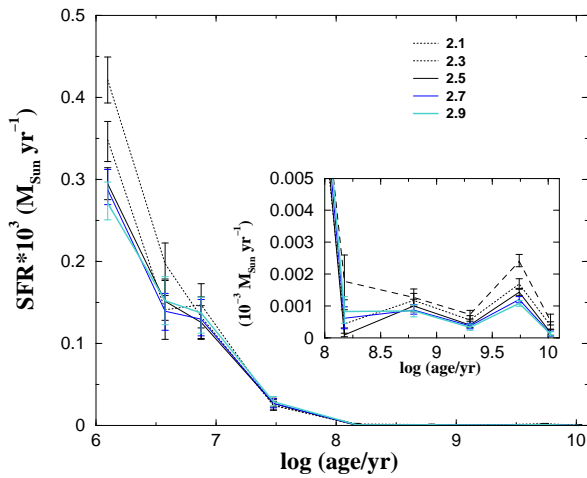


Fig. 16.— Recovered SFH for different assumptions on the IMF exponent.

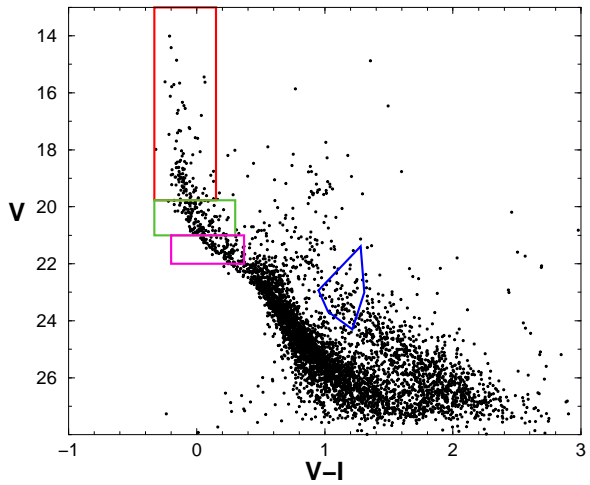


Fig. 17.— CMD regions used to constrain the IMF (see text).

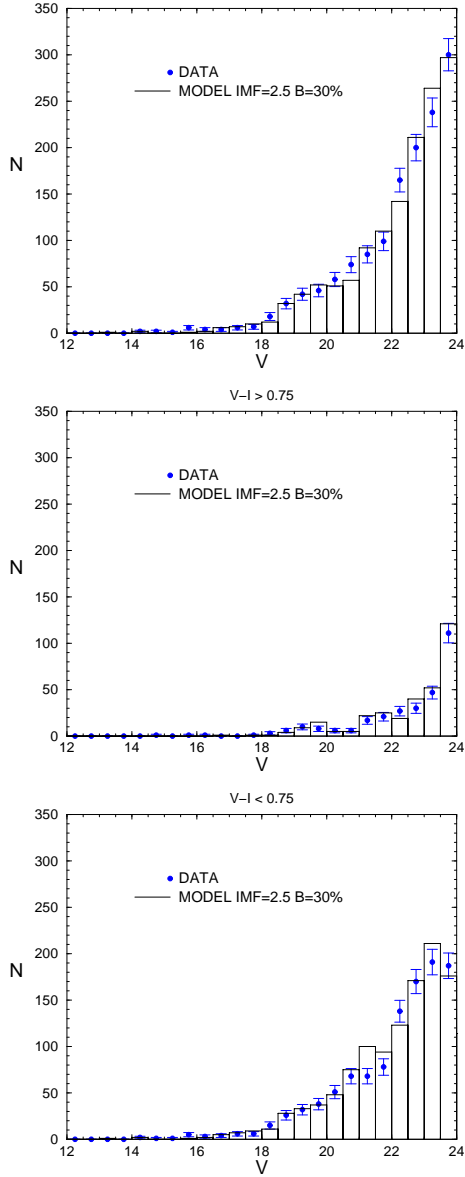


Fig. 18.— Simulated (IMF exponent  $\alpha = 2.5$  and binary fraction 30%) versus observational luminosity function for the whole sample (top panel), stars with  $V - I > 0.75$  (middle panel), stars with  $V - I < 0.75$  (bottom panel).

Unfortunately, the small size of our sample does not allow us to put tighter constraints.

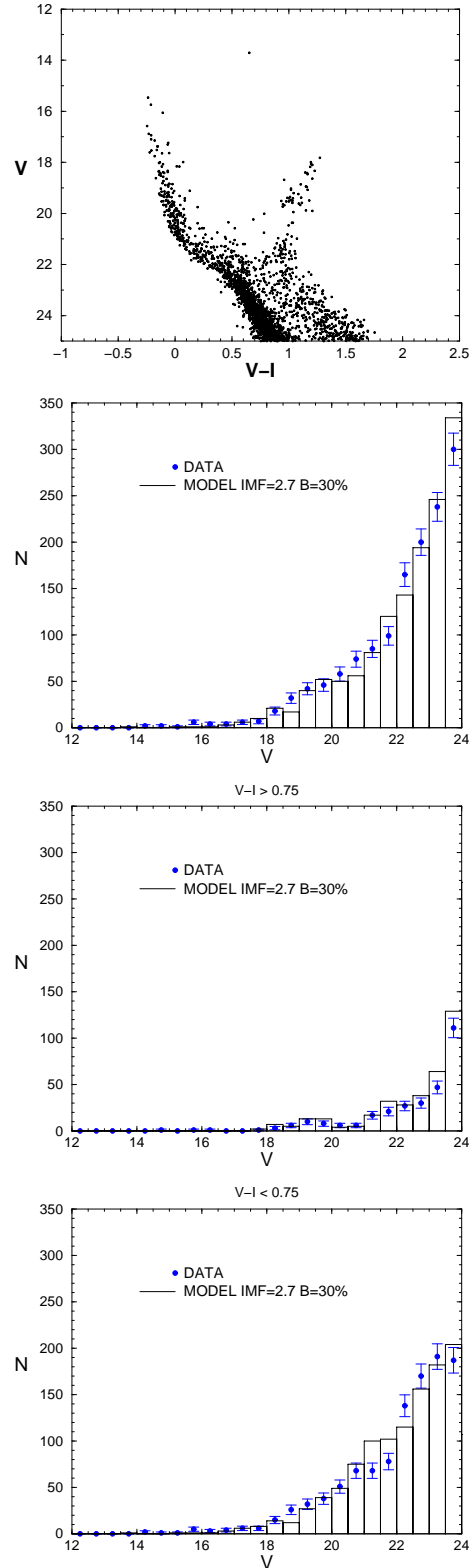


Fig. 19.— The top panel shows the best synthetic diagram using an IMF exponent  $\alpha = 2.7$ . The remaining figures follow the same criteria of Figure 18 but for  $\alpha = 2.7$ .

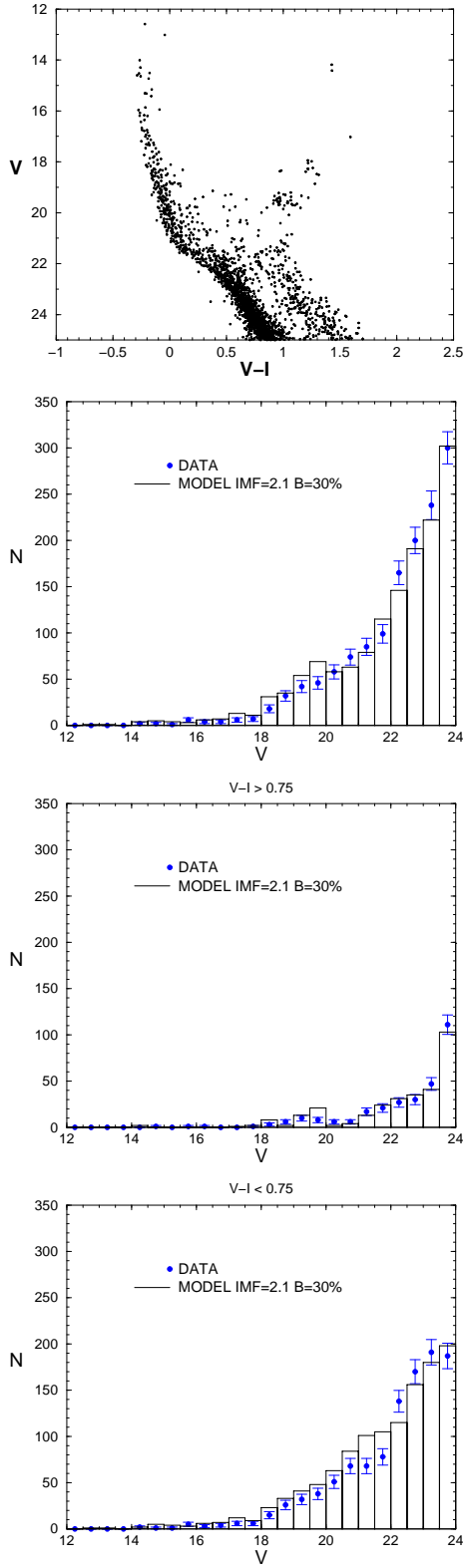


Fig. 20.— As in Figure 19 but for  $\alpha = 2.1$ .

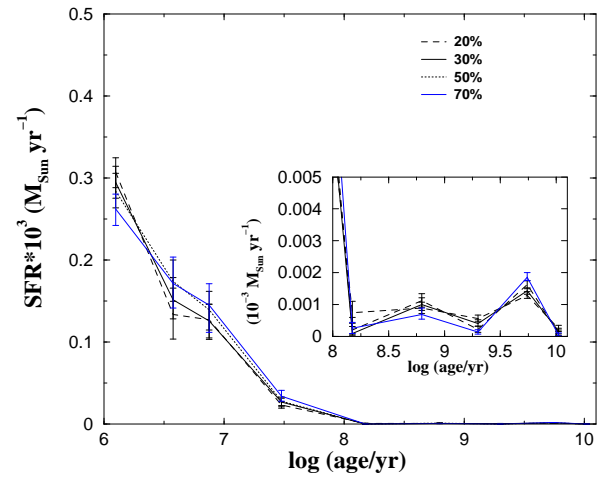


Fig. 21.— Recovered star formation rate adopting different binary fractions (the IMF exponent is fixed to 2.5).

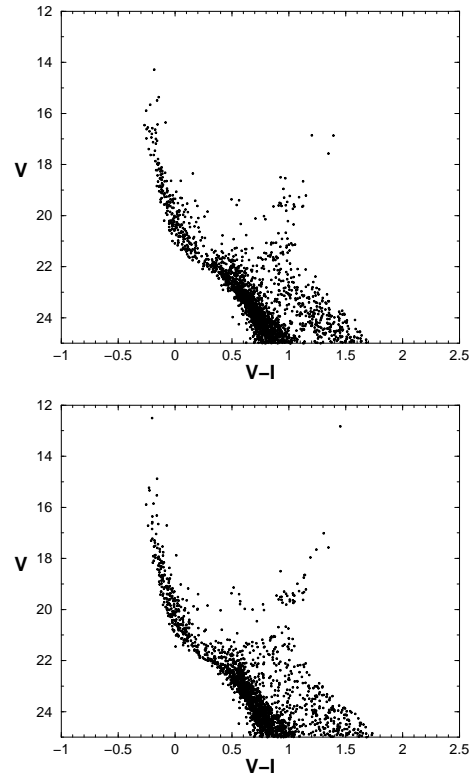


Fig. 22.— Synthetic CMD:  $\alpha = 2.5$ , binary fraction of 50% (top panel) and 70% (bottom panel).

TABLE 1A—*Continued*

Age (yr)	$\text{Log}(L/L_{\odot})$	$\text{Log}(T_{eff})$	Age(yr)	$\text{Log}(L/L_{\odot})$	$\text{Log}(T_{eff})$	Age(yr)	$\text{Log}(L/L_{\odot})$	$\text{Log}(T_{eff})$
0.20E+06	1.226	3.713	0.20E+06	1.516	3.727	0.20E+06	1.892	3.742
0.30E+06	1.121	3.716	0.30E+06	1.444	3.734	0.30E+06	2.054	3.768
0.40E+06	1.048	3.719	0.40E+06	1.416	3.739	0.40E+06	2.222	3.845
0.50E+06	0.994	3.721	0.50E+06	1.439	3.746	0.50E+06	2.414	3.956
0.60E+06	0.953	3.723	0.60E+06	1.519	3.756	0.60E+06	2.562	4.068
0.70E+06	0.922	3.725	0.70E+06	1.630	3.768	0.70E+06	2.644	4.167
0.80E+06	0.898	3.727	0.80E+06	1.720	3.785	0.80E+06	2.626	4.230
0.10E+07	0.867	3.731	0.10E+07	1.910	3.869	0.10E+07	2.456	4.237
0.20E+07	1.023	3.764	0.20E+07	2.016	4.163	0.11E+07	2.445	4.234
0.30E+07	1.380	3.856	0.21E+07	2.002	4.160			
0.50E+07	1.388	4.045						
0.61E+07	1.349	4.041						
$5.00 M_{\odot}$			$5.50 M_{\odot}$					
0.10E+05	2.498	3.700	0.10E+05	2.556	3.700			
0.20E+05	2.382	3.707	0.20E+05	2.460	3.709			
0.30E+05	2.313	3.712	0.30E+05	2.406	3.714			
0.50E+05	2.248	3.722	0.50E+05	2.395	3.725			
0.70E+05	2.233	3.727	0.70E+05	2.487	3.736			
0.10E+06	2.315	3.740	0.10E+06	2.551	3.766			
0.20E+06	2.536	3.862	0.20E+06	2.893	4.006			
0.30E+06	2.843	4.060	0.30E+06	3.111	4.231			
0.40E+06	2.979	4.229	0.40E+06	3.042	4.325			
0.50E+06	2.913	4.302	0.49E+06	2.920	4.312			
0.62E+06	2.779	4.289						